Sideband cooling and coherent dynamics in a microchip multi-segmented ion trap

Stephan Schulz ‡, Ulrich Poschinger, Frank Ziesel, and Ferdinand Schmidt-Kaler

Universität Ulm, Institut für Quanteninformationsverarbeitung, Albert-Einstein-Allee 11, D-89069 Ulm, Germany

Abstract. Miniaturized ion trap arrays with many trap segments present a promising architecture for scalable quantum information processing. The miniaturization of segmented linear Paul traps allows partitioning the microtrap in different storage and processing zones. The individual position control of many ions - each of them carrying qubit information in its long-lived electronic levels - by the external trap control voltages is important for the implementation of next generation large-scale quantum algorithms.

We present a novel scalable microchip multi-segmented ion trap with two different adjacent zones, one for the storage and another dedicated for the processing of quantum information using single ions and linear ion crystals: A pair of radio-frequency driven electrodes and 62 independently controlled DC electrodes allows shuttling of single ions or linear ion crystals with numerically designed axial potentials at axial and radial trap frequencies of a few MHz. We characterize and optimize the microtrap using sideband spectroscopy on the narrow $S_{1/2} \leftrightarrow D_{5/2}$ qubit transition of the $^{40}\mathrm{Ca}^+$ ion, demonstrate coherent single qubit Rabi rotations and optical cooling methods. We determine the heating rate using sideband cooling measurements to the vibrational ground state which is necessary for subsequent two-qubit quantum logic operations. The applicability for scalable quantum information processing is proven.

PACS numbers: 37.10.Ty, 37.10.-x, 32.80.Qk, 03.67.Lx

‡ corresponding author: stephan.schulz@uni-ulm.de

Contents

1. Introduction

Long term goal of our research is the large-scale quantum computer [1, 2] with multiple ions and linear ion crystals for encoding complex entangled states, with optimized laser pulses for processing quantum information (QIPC), and with well suited time-dependent trap control voltages to shuttle quantum information between a central processing unit and quantum memories or qubit read-out sections. On the way towards this goal we present in this paper the most complex microstructured ion trapping device with a large number of control segments such that in future order of 10^2 qubits might be processed. Currently we do not exploit at all the complexity of our segmented trapping device and the corresponding options for large-scale quantum processing. The purpose of this paper, however, is describing the trap device, characterizing its basic performance and proving necessary building blocks for quantum gates with ions.

The work presented here should be seen in context with pioneering work to fabricate specialized ion microtraps for QIPC (instead of using mm-sized conventional designs [3, 4, 5, 6]) by using microscale planar [7, 8], linear three-dimensional [9, 10, 11] or even more complex geometries [12]. Gold plated substrates allow electrode structures with gaps of a few μm, but semiconductor structuring may allow in future even finer and more complex traps [13]. Shuttling protocols for single ions [14, 15, 16, 17] have been tested and even used for implementing quantum algorithms [18, 19]. On the other hand, the application of well controlled laser pulses has lead to the entanglement of up to eight ions [20] and the realization of complex quantum algorithms like e.g. teleportation [21].

The paper is organized as follows: First we outline the steps for the fabrication of the multi-segmented linear ion trapping device and the integration in the overall experimental setup. Cold crystals of trapped $^{40}Ca^+$ ions are showing the elementary operation of this device. For refined studies of trapped ions and the properties of the trap we employ quantum jump spectroscopy on the narrow quadrupole transition, where all components of the ion motion are resolved easily. Investigating the micromotional sideband allows shifting of the ion to the center of the radio-frequency (RF) trapping field. Since we are observing a very small variation of the necessary compensation voltage only we conclude that charging effects are indeed effectively impeded by the advanced trap construction. If the ion is excited by a narrow band laser source, we observe Rabi flopping as we vary the pulse duration. Finally, we study the secular sidebands and sideband cool a single ion from Doppler temperature down to the vibrational ground state. Cooling time and trap heating time are revealed. In the outlook finally we sketch future applications.

2. Microchip Ion Trap

The Ulm microchip trap is a two layer electrode design modeled as logical continuation of conventional linear Paul traps (Fig. 1a). The storage zone is connected to the processing zone by a multi-segment transfer region in order to achieve a smooth passage avoiding vibrational excitation (Fig. 1b). The electrode layers are as symmetric as possible for well-balanced electric potentials on the trap axis such that micromotion should be minimized. Thus, the non-segmented RF segments are cut with notches precisely opposite to the separation cuts in the DC electrodes to improve the axial electric field symmetry. The microtrap is assembled in a UHV compatible ceramic chip carrier with the advantage of an exceptional alignment precision of the electrode layers. Furthermore easy electric connectivity, exchange usability and in the near future the integration in UHV compatible electronics boards with fast digital-analog converters and digital rf-synthesizers prioritize this proof of concept.

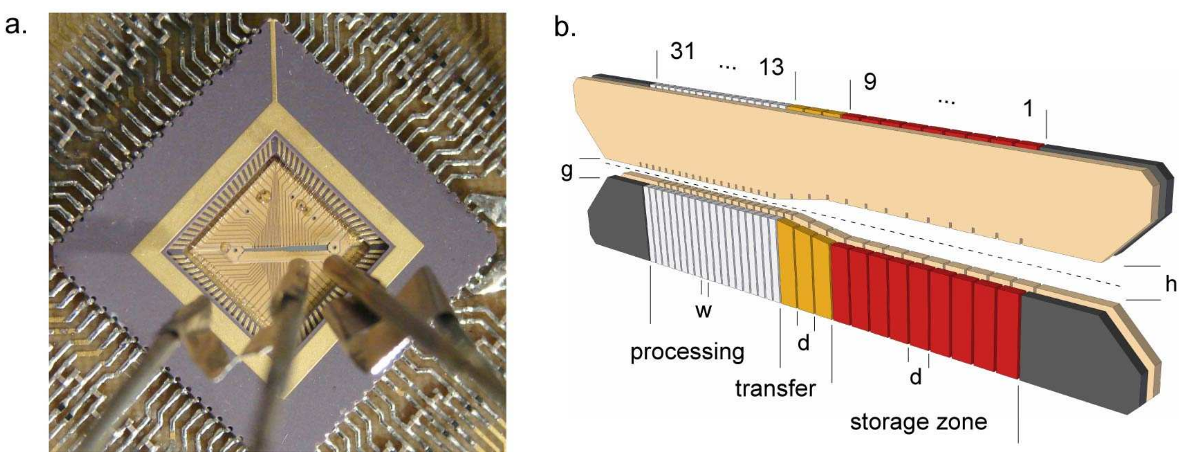

Figure 1. (a) Ulm microchip trap installed in the vacuum housing and connected to the filter board. In the front are the two calcium ovens. (b) Scheme of the trap: 31 electrode pairs of the different zones for storage, tranfer and processing are characterized by the slit width g,h and the electrode dimensions w,d.

2.1. Design and Fabrication

The Ulm microtrap is based on a geometric three-layer stack design fabricated using gold coated and laser cutted Al_2O_3 wafers§. The development process of the wafers starts with micro-machining of the blank 2-inch squared wafers (Fig. 2a) using a femtosecond pulsed laser source‖. In the storage zone the central slit width is h=500μm, while the transfer region narrows the slit to g=250μm according to the width of the processing zone (Fig. 1b). The central slit in the storage/transfer zone and the processing zone is bounded by the DC electrode fingers with a width of d=250μm and w=125μm separated

§ Reinhardt Microtech AG, Wangs, Switzerland
‖ Micreon GmbH, Hannover, Germany

with a spacing of 30μm. The constant length of the DC electrode fingers is 100μm. The length of the RF notches is 50μm with a 30μm spacing. Additional holes with a diamete of 40μm in the outer region allows alignment and mounting.

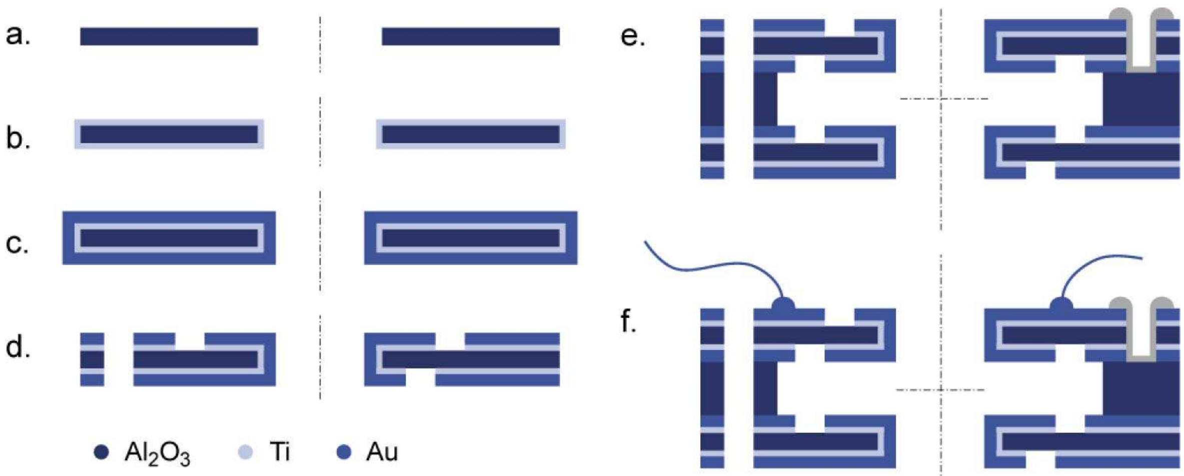

Figure 2. Fabrication process of the microtrap: Processing of the Al_2O_3 wafer includes laser machining (a), cleaning and coating (b)/(c) and laser cutting (d). Assembly includes mounting (e) and bonding (f).

The wafer metallization is done after a careful ultrasonic cleaning procedure (acetone, isopropyl, piranha) and an oxygen plasma cleaning. The blank laser cutted Al_2O_3 wafer is coated in an electron beam evaporator during a continuous rotation with 50nm titanium and 500nm gold (Fig. 2b,c). A declination angle of 45° is required during the coating process for an overall continuous coating. The surface roughness is better than 10nm, which was verified by atomic force microscopy. The conductor paths are manufactured by laser-structuring of the wafer metallization (Fig. 2d). Finally, the wafer is laser diced. Bottom, center and top layer of the microtrap are aligned and mounted with UHV compatible UV epoxy adhesive (Fig. 2e). The stack of three layers is mounted in a center holed UHV compatible leadless ceramic 84-pin chip carrier¶ with outer dimensions of 30mm squared and an inner cavity size of 12mm. Electrical connections to the ceramic chip carrier rely on ball bonding with 15μm diameter gold wire (Fig. 2e). Our design avoids dielectric blank Al_2O_3 areas, unavoidable isolation lines between the electrode segments are shifted away $>$100μm from the ions position by the extended electrode finger design. From an electron microscopy analysis we checked that the DC electrode finger segments are gold-plated completely from all sides.

The microtrap chip carrier is mounted on a low-pass filter printed circuit board (PCB), that serves as electrical connector device of the 80-pin ribbon cables. The PCB is based on the UHV compatible polyimide laminate Isola P97+, which is 200μm gold electroplated. The UHV compatible Capton ribbon cables are connected with ceramic

¶ Kyocera, type LCC8447001
+ Isola GmbH, Düren, Germany

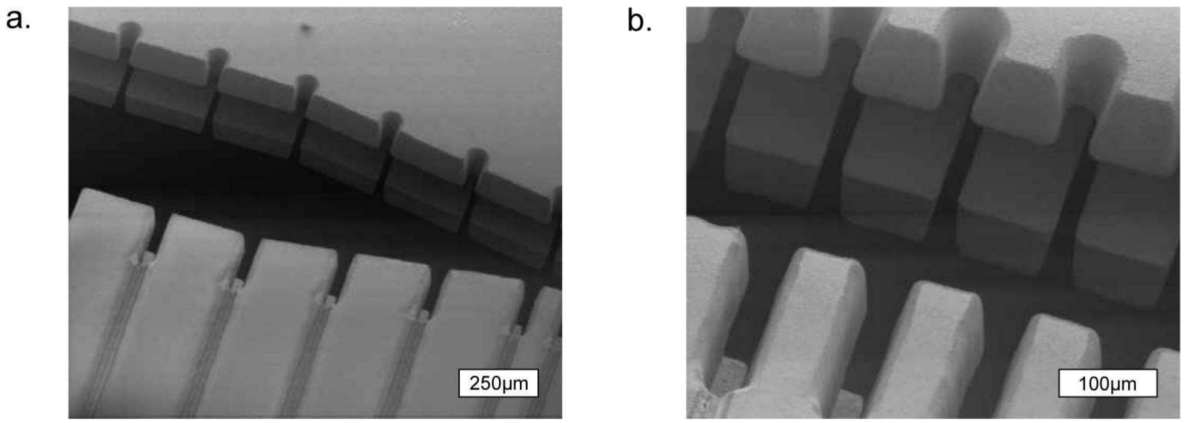

Figure 3. Electron microscope picture of the loading region (a) and narrower processor region (b). The gold-coated finger structure and the laser cuts to define electrodes are visible.

D-type connectors in vacuum. RC low-pass filters (ceramic SMD type) with a cutoff close to 10MHz are soldered close to the chip carrier (Fig. 1a).

Decreasing electrode geometries of the processing zone compared to the storage zone of the microtrap has some advantages with respect to quantum information experiments: A smaller electrode design provides stronger confinement of the ions at the same voltage levels. Stronger confinement leads to higher axial in radial vibration frequencies, which set the time scale for multi-qubit gate operations. For the details of the trapping fields in axial and radial direction we use numerical simulations.

2.2. Field Simulations

The trap region of the microtrap is partitioned into a 9 segment loading and storage section, a 3 segment transfer region and a 19 segment processing zone. Each electrode of a segment pair is voltage controlled separately, providing a full control for each trap site individually and an effective micromotion compensation. Numerical simulations give insight how to form potentials suitable to trap single ions or linear crystals (Fig. 4). The loading zone is optimized such that a thermal beam of Calcium passes through, therefore the cross section of the storage zone is asymmetric with a ratio 4:1. The more symmetric cross section of the processing zone with a ratio 2:1 leads to a strong confinement of the ions and higher radial and axial frequencies [22].

The two-dimensional dynamical confinement in the radial cross section at the storage region (Fig. 4a) is described numerically by the quadrupol potential strength of the dynamical trap potential ϕ. The lowest-order approximation $\phi = c_2/2\,(y^2 - z^2) \cdot U(t)$ shows the geometric factor c_2 of the quadrupol potential strength (yz cross section). The storage region is characterized by $c_2 = 0.52 \cdot 10^7\,m^{-2}$, the processing region shows a stronger confinement with $c_2 = 1.99 \cdot 10^7\,m^{-2}$. The dimensionless stability parameter $q = 2U/(m\Omega^2)\,c_2$ results. Under typical operation conditions, see Sect. 3.1, this results in $q = 0.14$ for the storage and $q = 0.55$ for

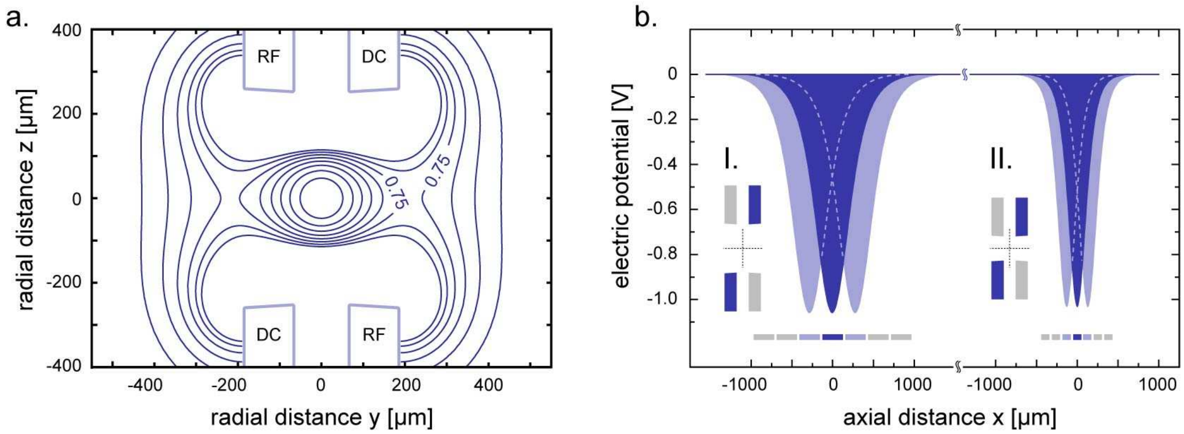

Figure 4. Numerical field simulation of the microtrap: (a) The pseudopotential cross section of the loading region shows equi-pseudopotential lines at 0.125eV, 0.25eV, 0.375eV, 0.5eV, 0.625eV and 0.75eV for a $^{40}Ca^{+}$ ion trapped at $\Omega = (2\pi)$ 24.841MHz with U_{pp}=140V. The trap depth is 0.755eV. (b) The axial potential is plotted along the trap axis in the loading (I) and processing (II) region. The individual electric potential of a single electrode pair at -5V (other electrodes at 0V) is shown for three adjacent electrode pairs.

the processing region. The calculated simplified frequency of the secular motion $\omega = \Omega \cdot q/2\sqrt{2}$ in the storage region is $\omega = 1.26$MHz and is reproduced experimentally with high accuracy.

The axial potential along the trap axis is calculated in a numerical three-dimensional electric potential simulation (Fig. 4b). Requirements for fast ion transport are deep axial potentials with moderate control voltages and a large spatial overlap of the axial potentials of adjacent electrode pairs [22]. The peak width at half-height of the axial potentials are 500μm at the storage region (250μm segment width) and 264μm at the loading region (100μm segment width). For the wider segments of 250μm in the storage zone the trap allows a tight confinement with an axial frequency of 1.20MHz with -5V applied only, which is experimentally verified within 5% accuracy via sideband spectroscopy.

3. Experimental Setup

3.1. Trap operation

For the RF supply of the trap a RF synthesizer is used, followed by a RF amplifier to feed +26dBm ($\sim$ 400mW) power into a helical resonator matching the 50Ω amplifier output impedance with the trap. The injected RF power is monitored by an capacitive divider. Under typical operating conditions we reach amplitudes of 280V_{pp} at a frequency of 24.841MHz. The DC electrodes are supplied with voltages in the range of $\pm$10V. The trap is installed in a stainless steel DN200CF vacuum chamber with a regular octagon DN63CF viewport symmetry. With a pump system comprising an 75l ion pump and a titanium sublimation pump we operate the experiment at a pressure of 10^{-10}mbar. Pairs of magnetic field coils in a three-axis Helmholtz-configuration are used for compensating the stray magnetic fields and generating a quantization axis with a magnetic field of 0.3mT directed at 45° with the trap axis x.

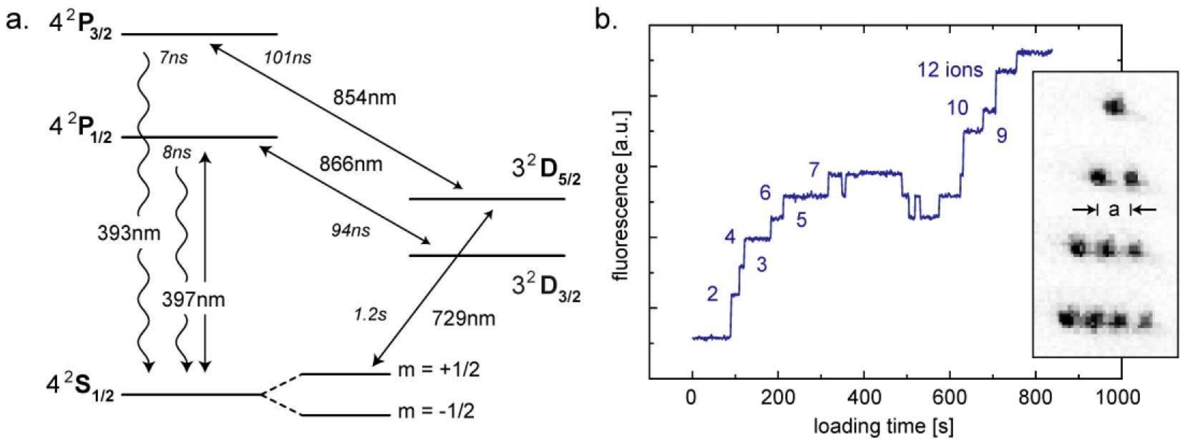

Figure 5. (a) Relevant levels, transition wavelengths and lifetimes in $^{40}Ca^{+}$. (b) Fluorescence near 397nm during loading observed with the EMCCD camera. The distance a of two ions results in 7μm.

3.2. Laser Configuration

Single ^{40}Ca^{+} ions stored in the trap are generated by photoionization of a neutral calcium atomic beam from a resistively heated oven. The two step process is driven by laser light near 423nm and 375nm [23]. Fig. 5a shows the level scheme of ^{40}Ca^{+}. Dipole transitions $4^2S_{1/2} \rightarrow 4^2P_{1/2}$ at 397nm allow for Doppler cooling of the ions, the $3^2D_{3/2} \rightarrow 4^2P_{1/2}$ transitions near 854nm and $3^2D_{5/2} \rightarrow 4^2P_{3/2}$ and 866nm for the depletion of the metastable D-levels. The quadrupole transition near 729nm from the $4^2S_{1/2}$ ground state to the metastable $3^2D_{5/2}$ level is employed for sideband spectroscopy, sideband cooling and coherent quantum dynamics.

All transitions of the ^{40}Ca^{+} ion are driven by grating stabilized diode lasers. The lasers at 397nm, 866nm and 854nm are locked to external Zerodur Fabry-Perot cavities (finesse F=250) for frequency stability using the Pound-Drever-Hall (PDH) technique. The laser at 729nm (diode followed by a tapered amplifyer) is PDH-locked to a ULE cavity (F$\geq$50000) reaching a sub-kHz linewidth. Lasers at 866nm, 854nm and 729nm can be switched off using acousto-optical modulators in double-pass configuration, also being employed for tuning the laser frequency near 729nm. Laser beams intersect the trap under 45° with respect to the trap axis x. A separate $\sigma+$ beam is deviated from the laser near 397nm for optical pumping and intersects the trap under -45°, parallel with the magnetic field direction. The beam near 729nm is focused to a waist size of 15μm and intersects the trap perpendicular to the magnetic field axis under 45°, yielding a Lamb Dicke factor of excitation of η_{729}=6.5% for $\omega_{ax.}$=1.1MHz. The polarization at

729nm is chosen such that only Δm=2 transitions are allowed, e.g. from $S_{1/2}$, m=+1/2 to $D_{5/2}$, m=+5/2 and m=-3/2.

3.3. Doppler Cooling, Fluorescence Detection and Cold Ion Crystals

The ion fluorescence is imaged by a custom lens system* (focal length 66.8mm, numeric aperture 0.27) on an EMCCD camera♯ (efficiency of 50%) and a photomultiplier tube (PMT) of quantum efficiency ∼27% for detecting ions and reading out the quantum state. The magnification of the imaging branch is roughly 20. The fluorescent light is collected from a solid angle of ∼2.5%. It is distributed at a ratio of 80:20 between PMT and camera by a beam splitter and filtered by a band pass filter to suppress background photons. For trapping and cooling, 1mW of 866nm light is focussed to 30μm. The power of the laser near 397nm is focussed to a spot size of 20μm and can be switched between zero, a reduced power level of 30μW (Doppler cooling) and full power with about 300μW (detection). With the laser slightly red detuned and proper micromotion compensation, a single ion count rate of 16kHz at a background of 4kHz can be achieved with the PMT. If an ion is shelved in the long lived $D_{5/2}$ level, no light is scattered. With a detection time of 5ms, we are able to discriminate the qubit states with an error probability of $3 \cdot 10^{-3}$ [5]. Fig. 5b shows linear ion crystals trapped and observed in the microtrap.

4. Quantum Jump Spectroscopy

Quantum jump spectroscopy has been used to determine the frequency of clock transitions with an accuracy of about 7 parts in 10^{-17} [24, 25, 26, 27]. A narrow dipole forbidden transition is driven and subsequently the excitation to the metastable level is tested by exposure to resonant radiation on a dipole allowed transition.

4.1. Sideband spectroscopy on the $S_{1/2}$ to $D_{5/2}$ transition

In the experiments presented here, we perform spectroscopy on the $S_{1/2}$ to $D_{5/2}$ transition. With a lifetime of 1.2s, the spectroscopic resolution is limited by the laser pulse duration, the Rabi frequency during the excitation and the frequency stability of the laser source. The harmonic motion of the ion in the trap can be spectroscopically investigated at the level of single vibrational quanta. The electronic and vibrational state is manipulated coherently with the following sequence:

(i) Doppler cooling: The laser near 397nm is red detuned from the $S_{1/2}$ to $P_{1/2}$ transition to $\lesssim$1/2 of the fluorescence rate. This corresponds to a setting of about $\Gamma/2$ where $\Gamma=(2\pi)22.3$MHz is the natural linewidth of the dipole transition. The beam is attenuated in order to avoid saturation. The laser frequency near 866nm

* Sill Optics, Wendelstein, Germany
♯ iXon DV860-BI, Andor Technology, Belfast, Northern Ireland

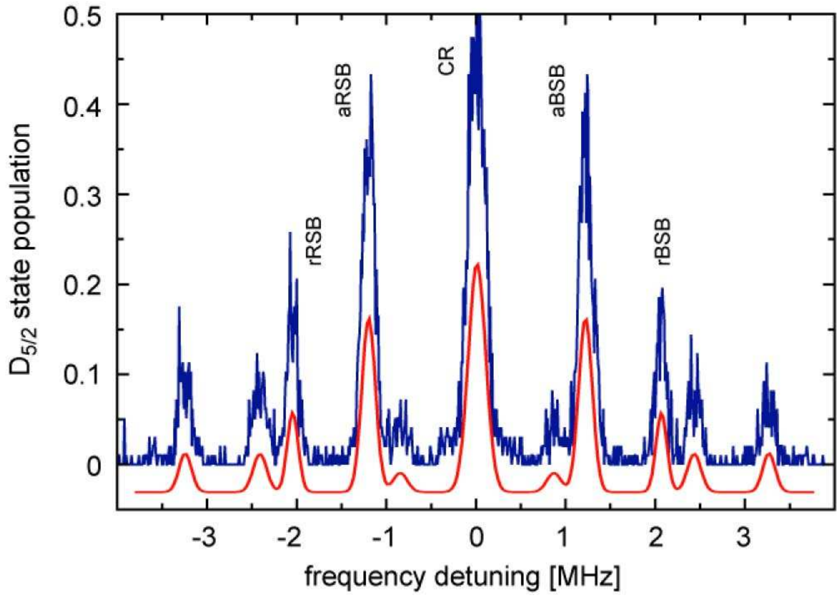

Figure 6. Quantum jump spectroscopy with a single ion: The laser frequency near 729nm is scanned over the carrier transition and the vibrational sidebands. For the data shown here, we have used a laser linewidth of ∼200kHz. The fit to the data (shifted and downsized for clarity) determines the axial and radial trap frequencies, $\omega_{\rm ax}$= (2π)1.2MHz and $\omega_{\rm rad}$= (2π) 2MHz.

is tuned for maximum fluorescence. Additionally, resonant laser light depopulates the metastable $D_{5/2}$ level. Typically we apply Doppler cooling for 5ms. While the theoretical cooling limit results in a mean phonon number of $\overline{n}$ $\hbar\omega_{\rm trap} = \Gamma/2$, with $\overline{n}$ ∼11, typically we observe a slightly higher $\overline{n}$ between 15 and 25.

(ii) Optical pumping: With a typically 5μs short pulse of $\sigma+$ polarized light near 397nm we pump the ion into the $S_{1/2}$, m=+1/2.

(iii) Sideband cooling (optionally): We tune the laser light near 729nm such that the red secular sideband of the $S_{1/2}$, m=+1/2 to $D_{5/2}$, m=+5/2 is excited. The $D_{5/2}$ state is quenched by resonant laser light near 854nm to the $P_{3/2}$ which quickly decays to $S_{1/2}$ closing the cooling cycle. Short pulses of optical pumping as in step (ii) are inserted into, and also conclude the sideband cooling.

(iv) Spectroscopy pulse: All laser sources, except the laser light near 729nm, are switched off. We excite the $S_{1/2}$, m=+1/2 to $D_{5/2}$ transition with pulses of well defined frequency, duration and intensity.

(v) State detection: The lasers at 397nm and 866nm are switched back on. The power of the 397nm laser is at maximum such that a maximum count rate is obtained. The PMT counts photons of the ions fluorescence. If the ion had been excited on the quadrupole transition to the $D_{5/2}$, no fluorescence photons will be observed.

The entire sequence is repeated typically 50 to 500 times depending on the requirements, and the average excitation to the $D_{5/2}$ level is recorded. For

N measurements and an excitation probability p, the projection noise error is given by $\sqrt{p(1-p)/N}$. Then e.g. the laser frequency near 729nm is varied, see Fig. 6. Here, the ion is excited without sideband cooling step (iii) such that the radial and axial red and blue motional sidebands show equal strength. These resonances are denoted with rRSB to rBSB. Additional resonances show up at a laser detuning for a second-sideband excitation $\pm 2\omega_{\rm ax}$ and at difference frequencies of sidebands $\omega_{\rm rad} - \omega_{\rm ax}$.

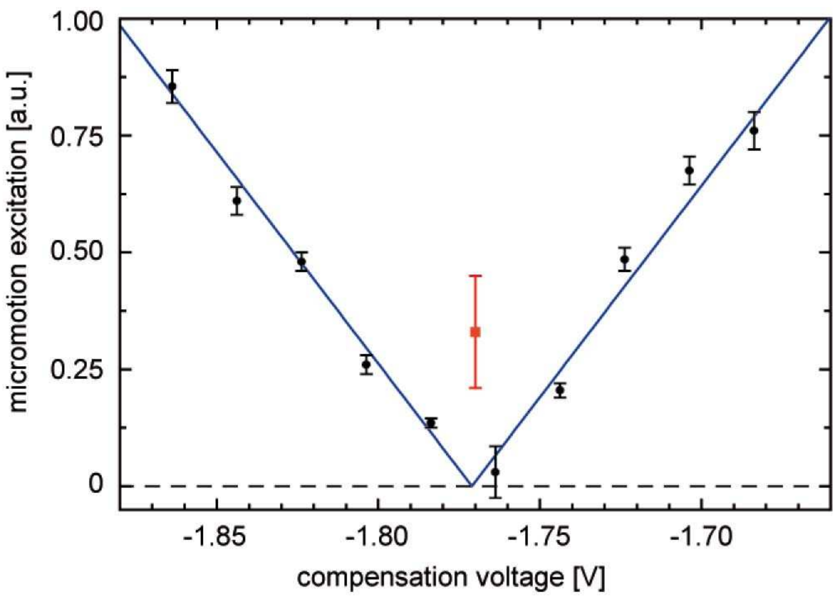

Figure 7. Excitation on the micromotional sideband for compensation: The amplitude of the excitation line is plotted as the compensation voltage is varied. For comparison the excitation amplitude of the carrier with a laser power reduced by a factor of 10 (indicated by the red square data point).

4.2. Micromotion Compensation

If an ion is displaced from the node of the rf electric field either by asymmetries or by patch charges, it will oscillate at the trap drive frequency. Consequently, Doppler cooling and fluorescence detection will be affected. However, micromotion is compensated by applying a balanced voltage difference to the particular segments of an electrode pair such that the ion is moved into the RF trap center. Various methods of measuring the micromotion have been studied [28], yet another method uses sideband spectroscopy: We excite the sideband at $\omega_{\rm carrier} + \Omega$ and compare the sideband excitation with that on the carrier [5]. The Rabi frequency Ω_1 on the micromotion sideband and that one on the carrier Ω_0 holds $\Omega_1/\Omega_0 = \mathrm{J}_1(\mathrm{m})/J_0(\mathrm{m}) \approx \beta/2$ for $\beta \ll 1$. As the excitation to the $\mathrm{D}_{5/2}$ state is proportional to Ω^2 such for low saturation, we can measure the ions micromotion directly, see Fig. 7. We find the minimum excitation close to -1.77V. At this minimum, thus for optimum compensation voltage, we reduce the ratio of excitation strength to zero with an error of ± 0.03. This measured value corresponds to the ratio of squared Bessel functions $\mathrm{J}_1^2(\mathrm{m})/\mathrm{J}_0^2(\mathrm{m})$ with modulation index of 0.0 ± 0.17, which is due to a residual micromotion oscillation amplitude $x_{min} = \beta_{min}(\lambda/2) = (0.0 \pm 0.17)(729\text{nm}/2)$ of 0.0±130nm. The optimal compensation voltage changes by less than 0.5% from day to day.

In conclusion, the micromotion can be nulled by a properly set compensation voltage and, due to the shielding effect of the gold coated finger shaped electrodes, stray electric fields from isolating parts of the microtrap do not show up with large and fluctuating contributions.

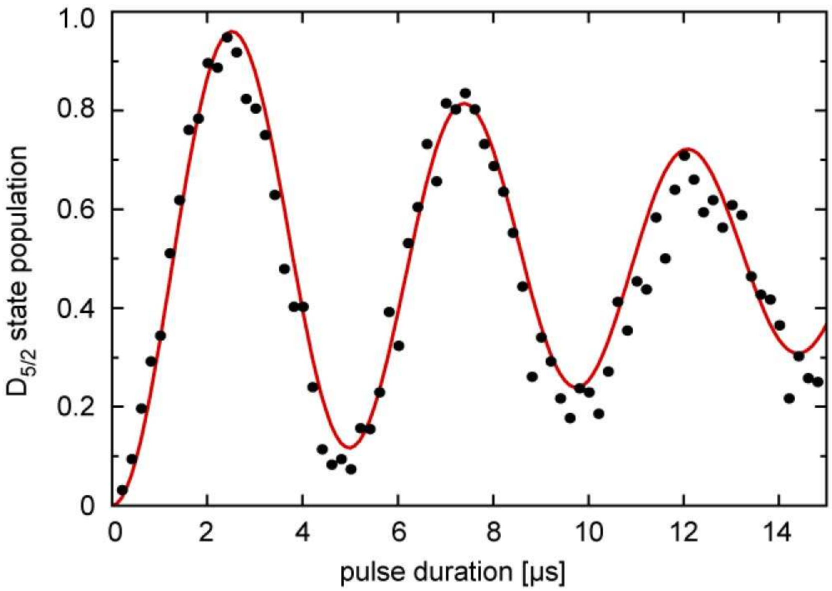

Figure 8. Rabi oscillation with a single ion on the carrier transition. The data are taken with a laser power of ∼60mW. The model curve assumes the dephasing of the oscillation due to a thermal distribution with a mean phonon number of 12.

4.3. Coherent Single Ion Dynamics

The coherent ion-light interaction leads to Rabi oscillations between the $S_{1/2}$ ground state and the excited metastable $D_{5/2}$ state when the duration of the interaction is varied. If the single ions internal states are used to store qubit information, a π-pulse will flip the qubit between the two logic states.

Here we present Rabi oscillations on the carrier transition for a single ion, see Fig.8, which has been Doppler cooled. The data shows a 95% efficiency for the π-pulse at 2.5μs, corresponding to a Rabi frequency of $\Omega_0 = (2\pi)$ 200kHz. The decay of contrast is due to the fact that we observe an incoherent superposition of Rabi oscillations with a different frequency for each thermally occupied Fock state: $\Omega_{n,n} \propto 1 - \eta_{729}^2 n$. If we model the data with $P_D(t) = \sum p_n(\overline{n})\sin^2(\Omega_{n,n}(t))$ we find agreement for a thermal distribution p_n with $\overline{n}$ ∼11.

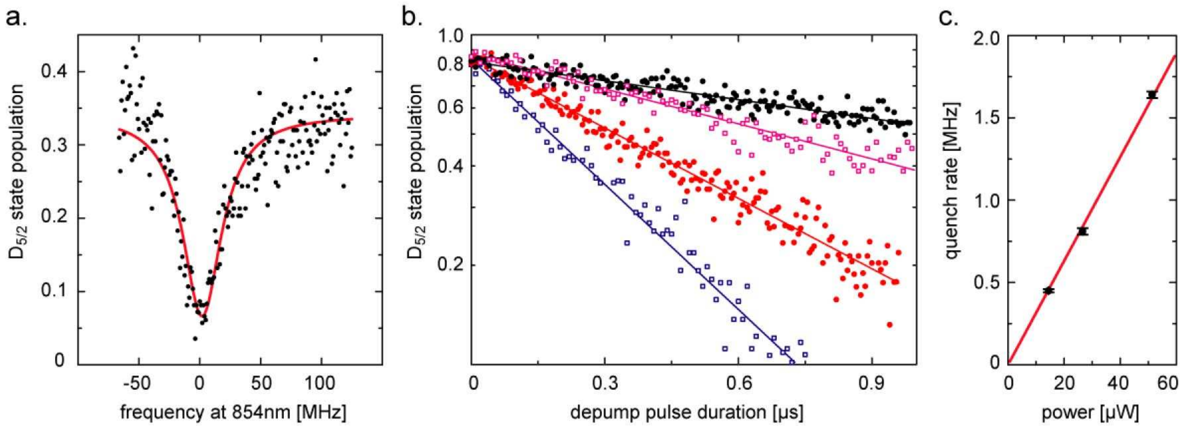

Figure 9. a) Depletion of the $D_{5/2}$ state by a 3μs pulse near 854nm. The observed dip corresponds the resonance line and allows for tuning the laser to resonance. We model the data by a 37MHz power broadened Lorentzian. b) After a π-pulse on the carrier transition at 729nm, the depletion pulse length to the $P_{3/2}$ state is scanned. The exponential decay fit determines γ_{eff}, here plotted with four different laser powers at 854 nm. c) The dependence of γ_{eff} is plotted as a function of the 854nm laser power, a linear fit yields 31.6(5)kHz/μW.

4.4. Sideband Cooling

For Doppler cooling, the temperature limit is given by the natural linewidth of the dipole transition. For quantum logic operations, however, a mean phonon number below this limit is often required. Therefore we apply sideband cooling on the narrow $S_{1/2}$ to $D_{5/2}$ transition [29]. Laser radiation near 729nm on the red sideband of the transition excites from $S_{1/2}$, m=+1/2 to $D_{5/2}$, m=+5/2. The effective width of this cooling transition can be increased by applying resonant laser light near 854nm. This mixes the $D_{5/2}$ state with the $P_{3/2}$ state which rapidly decays in the $S_{1/2}$, m=+1/2. The cooling rate is modified accordingly, and the effective width of the $D_{5/2}$ level sets an upper limit for the rate of cooling cycles.

For the introduction of laser cooling of trapped particles we apply the semiclassical theory [30], determine all laser cooling parameters experimentally and compare the cooling result with the theoretical expectation.

The theoretical limit of sideband cooling is given by the ratio of laser cooling Γ_{cool} and the heating rates $\Gamma_{\mathrm{heat}} = \Gamma_{\mathrm{laser-heat}} + \Gamma_{\mathrm{trap}}$, yielding $\overline{n} = \Gamma_{\mathrm{heat}}/(\Gamma_{\mathrm{cool}} - \Gamma_{\mathrm{heat}})$ as steady state average phonon number. Heating by laser processes is due to either an off-resonant excitation on the carrier transition with subsequent decay on the blue sideband or an off-resonant blue sideband excitation followed by a decay on the carrier [30]. A calculation of the detailed balance of phonon states leads to

$$\overline{n} = \left(\frac{\eta_{\mathrm{spont}}^2}{\eta_{729}^2} + \frac{1}{4} \right) \; \frac{\gamma_{\mathrm{eff}}^2}{4\omega} \tag{1}$$

if trap heating is excluded. Here, the parameter η_{spont}=0.17, for 1.1MHz trap frequency ω, takes the recoil into account if the ion decays spontaneously from the

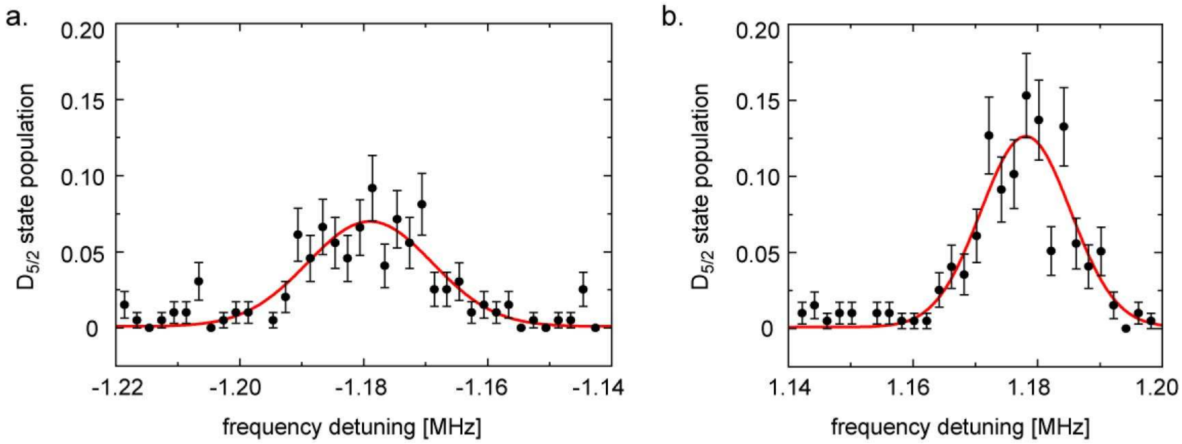

Figure 10. a) Sideband cooling of the axial vibration of a single ion. The imbalance of blue and red sideband leads to an estimation of a mean phonon number of 1.2(3). The spectrum has been measured with a 200μs delay after the sideband cooling. b) The trap heating is determined from a linear fit to the data, see Fig. 11.

$P_{3/2}$ level while η_{729}=0.065 is due to the laser recoil. Only the cooling rate, but not the cooling limit depends on the intensity of the laser near 729nm. $\gamma_{\rm eff}$ denotes the effective linewidth from quenching the $D_{5/2}$ state to the $P_{3/2}$ and is adjusted by the laser power at 854nm. The average phonon number increases with the intensity of the laser near 854nm, thus one has a tradeoff between cooling rate and minimum temperature. However, even for $\gamma_{\rm eff} \simeq 90$kHz, Eq. 1 predicts an almost perfect ground state of vibration with only $\overline{n} \leq 0.01$. The situation is more complicated if we take trap heating into account: The steady state photon number results from the balance

$$\overline{n} = \frac{\Gamma_{\rm laser-heat} + \Gamma_{\rm trap}}{\Gamma_{\rm laser-cool} - \Gamma_{\rm laser-heat} - \Gamma_{\rm trap}} \simeq \frac{\Gamma_{\rm trap}}{\Gamma_{\rm laser-cool} - \Gamma_{\rm trap}} \tag{2}$$

if the laser induced heating is small compared to the trap heating rate. We find that the thermal mean phonon number becomes

$$\overline{n} = \frac{\Gamma_{\rm trap}}{(\eta_{729}\Omega_{729}/\gamma_{\rm eff})^2 \;\; \gamma_{\rm eff} - \Gamma_{\rm trap}}, \tag{3}$$

for the case where the net cooling rate $W = (\eta\Omega)^2/\gamma - \Gamma$ is positive. In contrast to Eq. 1, the cooling limit now depends on the intensity of the laser near 729nm driving the red sideband of the quadrupole transition. We consider here the case where the sideband excitation is incoherent, with $\eta\Omega \leq \gamma$.

In order to compare the above cooling theory to the experiment, we need to determine $\gamma_{\rm eff}$, Ω_{729} and $\Gamma_{\rm trap}$ in independent experimental measurement sequences and compare the theoretical prediction in Eq. 3 with the experimental outcome on $\overline{n}$.

$\gamma_{\rm eff}$ is determined by controlled depletion of the metastable state: After Doppler cooling and optical pumping, we apply a 1μs laser pulse on the carrier transition such that the ion is transferred into $D_{5/2}$. A pulse of laser light resonant to the $D_{5/2}$ to $P_{3/2}$ transition is then applied and finally the remaining $D_{5/2}$ population is determined. From

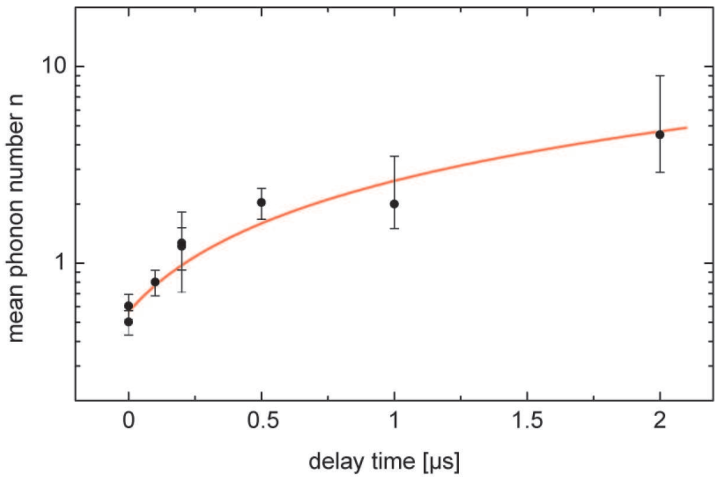

Figure 11. Heating rate measurement of the axial vibrational mode of a single ion as measured from the temperature increase after a delay time. The values of d$\overline{n}$/dt = 2.1(3) per ms and the minimum phonon number of 0.56(5) are determined from a linear fit to the data.

the exponential decay, see Fig. 9b, we determine the effective cooling width that is as expected a linear function of the laser power at 854nm, with $\gamma_{\text{eff}}[\text{kHz}] = 31.6(5)\text{P}_{854}[\mu W]$.

The Rabi frequency on the quadrupole transition is revealed from measurements such as in Fig. 8. With the maximum available laser power of 60mW we reach $\Omega_0 \simeq (2\pi)$ 200kHz. Correspondingly, the maximum possible sideband excitation with this laser power is $\eta\Omega_0 = (2\pi)$ 13kHz.

4.5. Heating Rate measurement

The mean phonon number of $\overline{n}$ is determined from spectra such as in Fig. 10 showing red and blue sideband after sideband cooling. From the asymmetry of excitation A=$\text{P}_{red}/\text{P}_{blue}$ we deduce the mean phonon number $\overline{n} = A/(1-A)$, here $\overline{n}$=0.56(5). To obtain the trap heating rate, we insert a variable waiting time interval between steps (iii) and (iv) in the experimental sequence, Sect. 4.1 [4]. The data plotted in Fig. **??** yields a trap heating of 2.1(3) per ms.

Note that quantum gate operations and the transport of ions in the trap are about 10 to 100 times faster than the measured trap heating. In future we will investigate the influence of the gold coating (different surface qualities and thickness) on the trap heating.

5. Conclusion and Outlook

We have outlined the design, the fabrication and the first characterization of a novel multi-segmented microchip ion trap, and we have show that this trap is suited for scalable quantum logic. In some detail, the sideband cooling on the quadrupole transition has been investigated. In future, we will explore Raman transitions between

Zeeman ground (qubit) states $S_{1/2}$ m=+1/2 and m=-1/2 for the cooling, for coherent qubit rotations and for two-qubit gate operations. Additionally, we will study the transport of quantum information between the processor and the memory section benefiting from the large number of trap segments. Further development will include the integration of micro optical elements.

Acknowledgements: We thank Frank Korte (Micreon GmbH) for his expertise in laser cutting, H. Roscher for the cooperation in the cleanroom facility, K. Singer and R. Reichle for their contributions in an earlier stage of the experiment, K. S. for his important help with the experimental control software, and J. Eschner for discussions. We acknowledge financial support by the German science foundation DFG within the SFB/TRR-21 and by the European commission within MICROTRAP (Contract No. 517675) and EMALI (Contract No. MRTN-CT-2006-035369).

[1] M. Nielsen and I.L. Chuang. *Quantum Computation and Quantum Information.* Cambridge University Press, 2000.

[2] European and the US quantum information roadmaps are found at http://qist.ect.it and at http://qist.lanl.gov.

[3] W. Neuhauser, M. Hohenstatt, P. Toschek, and H. Dehmelt. Optical-sideband cooling of visible atom cloud confined in parabolic well. *Phys. Rev. Lett.*, 41:233, 1978.

[4] C. Roos, Th. Zeiger, H. Rohde, H.C. Nägerl, J. Eschner, D. Leibfried, F. Schmidt-Kaler, and R. Blatt. Quantum state engineering on an optical transition and decoherence in a paul trap. *Phys. Rev. Lett.*, 83:4713, 1999.

[5] C. Roos. *Controlling the quantum state of trapped ions.* PhD thesis, Leopold-Franzens-Universität Innsbruck, 2000.

[6] F. Schmidt-Kaler, H. Häffner, S. Gulde, M. Riebe, G.P.T. Lancaster, T. Deuschle, C. Becher, W. Hänsel, J. Eschner, C. Roos, and R. Blatt. How to realize a universal quantum gate with trapped ions. *Appl. Phys. B*, 77:789, 2003.

[7] S. Seidelin, J. Chiaverini, R. Reichle, J.J. Bollinger, D. Leibfried, J. Britton, J. Wesenberg, R.B. Blakestad, R.J. Epstein, D. Hume, W.M. Itano, J.D. Jost, C. Langer, R. Ozeri, N. Shiga, and D.J. Wineland. A microfabricated surface-electrode ion trap for scalable quantum information processing. *Phys. Rev. Lett.*, 96:2530031, 2006.

[8] K.R. Brown, R.J. Clark, J. Labaziewicz, P. Richerme, D.R. Leibrandt, and I.L. Chuang. Loading and characterization of a printed-circuit-board atomic ion trap. *Physical Rev. A*, 75:15401, 2007.

[9] D. Stick, W. K. Hensinger, S. Olmschenk, M. J. Madsen, K. Schwab, and C. Monroe. Ion trap in a semiconductor chip. *Nature Physics*, 2:36, 2006.

[10] D. Leibfried and T. Schätz. Ein atomarer abakus. *Physik Journal*, 3:23, 2004.

[11] Q.A. Turchette, D. Kielpinski, B.E. King, D. Leibfried, D.M. Meekhof, C.J. Myatt, M.A. Rowe, C.A. Sackett, C.S. Wood, W.M. Itano, C. Monroe, and D.J. Wineland. Heating of trapped ions from the quantum ground state. *Phys. Rev. A*, 61:063418, 2000.

[12] W.K. Hensinger, S. Olmschenk, D. Stick, D. Hucul, M. Yeo, M. Acton, L. Deslauriers, C. Monroe, and J. Rabchuk. T-junction ion trap array for two-dimensional ion shuttling and storage and manipulation. *Appl. Phys. Lett.*, 88:034101, 2006.

[13] M. Brownnutt, G. Wilpers, P. Gill, R.C. Thompson, and A.G. Sinclair. Monolithic microfabricated ion trap chip design for scalable quantum processors. *New J. Phys.*, 8 No 10:232, 2006.

[14] M.A. Rowe, A. Ben-Kish, B. DeMarco, D. Leibfried, V. Meyer, J. Beall, J. Britton, J. Hughes,

W.M. Itano, B. Jelenkovic, C. Langer, T. Rosenband, and D.J. Wineland. Transport of quantum states and separation of ions in a dual rf ion trap. *Quantum Information and Computation*, 2:257–271, 2002.

[15] R. Reichle, D. Leibfried, R.B. Blakestad, J. Britton, J.D. Jost, E. Knill, C. Langer, R. Ozeri, S. Seidelin, and D.J. Wineland. Transport dynamics of single ions in segmented microstructured paul trap arrays. *Fortschr. Phys.*, 54:666, 2006.

[16] D. Hucul, M. Yeo, W.K. Hensinger, J. Rabchuk, S. Olmschenk, and C. Monroe. On the transport of atomic ions in linear and multidimensional ion trap arrays. *quant-ph/0702175*, 2007.

[17] G. Huber, T. Deuschle, W. Schnitzler, R. Reichle, K. Singer, and F. Schmidt-Kaler. Transport of ions in a segmented linear paul trap in printed-circuit-board technology. *accepted for publication New J. Phys.*, 2007.

[18] M.D. Barrett, J. Chiaverini, T. Schaetz, J. Britton, W.M. Itano, J.D. Jost, E. Knill, C. Langer, D. Leibfried, R. Ozeri, and D.J. Wineland. Deterministic quantum teleportation of atomic qubits. *Nature*, 429:737, 2004.

[19] R. Reichle, D. Leibfried, E. Knill, J. Britton, R.B. Blakestad, J. Jost, C. Langer, R. Ozeri, S. Seidelin, and D.J. Wineland. Experimental purification of two-atom entanglement. *Nature*, 443:838, 2006.

[20] H. Häffner, W. Hänsel, C.F. Roos, J. Benhelm, D. Chek al kar, M. Chwalla, T. Körber, U.D. Rapol, M. Riebe, P.O. Schmidt, C. Becher, O. Gühne and W. Dür, and R. Blatt. Scalable multiparticle entanglement of trapped ions. *Nature*, 438:643, 2005.

[21] M. Riebe, H. Häffner, C.F. Roos, W. Hänsel, J. Benhelm, G.P.T. Lancaster, T.W. Körber, C. Becher, F. Schmidt-Kaler, D.F.V. James, and R. Blatt. Deterministic quantum teleportation with atoms. *Nature*, 429:734, 2004.

[22] S. Schulz, U. Poschinger, K. Singer, and F. Schmidt-Kaler. Optimization of segmented linear paul traps and transport of stored particles. *Fortschr. Phys.*, 54:648, 2006.

[23] S. Gulde, D. Rotter, P. Barton, F. Schmidt-Kaler, R. Blatt, and W. Hogervorst. Simple and efficient photoionization loading of ions for precision ion-trapping experiments. *Appl. Phys. B*, 73:861, 2001.

[24] T. Rosenband, P.O. Schmidt, D.B. Hume, W.M. Itano, T.M. Fortier, J.E. Stalnaker, K. Kim, S.A. Diddams, J.C.J. Koelemeij, J.C. Bergquist, and D.J. Wineland. Observation of the $^1S_0$ to $^3P_0$ clock transition in $^{27}Al^+$. *Phys. Rev. Lett.*, 98:2208011, 2007.

[25] W.H. Oskay, S.A. Diddams, E.A. Donley, T.M. Fortier, T.P. Heavner, L. Hollberg, W.M. Itano, S.R. Jefferts, M.J. Delaney, K. Kim, F. Levi, T.E. Parker, and J.C. Bergquist. Single-atom optical clock with high accuracy. *Phys. Rev. Lett.*, 97:020801, 2006.

[26] H.S. Margolis, G.P. Barwood, G. Huang, H.A. Klein, S.N. Lea, K. Szymaniec, and P. Gill. Hertz-level measurement of the optical clock frequency in a single $^{88}Sr^+$ ion. *Science*, 306:1355, 2004.

[27] T. Schneider, E. Peik, and C. Tamm. Sub-hertz optical frequency comparisons between two trapped $^{171}Yb^+$ ions. *Phys. Rev. Lett.*, 94:230801, 2005.

[28] D.J. Berkeland, J.D. Miller, J.C. Bergquist, W.M. Itano, and D.J. Wineland. Minimization of ion micromotion in a paul trap. *J. Appl. Phys.*, 83:5025, 1998.

[29] I. Marzoli, J.I. Cirac, R. Blatt, and P. Zoller. Laser cooling of trapped three-level ions: Designing two-level systems for sideband cooling. *Phys. Rev. A*, 49:2771, 1994.

[30] S. Stenholm. The semiclassical theory of laser cooling. *Rev. Mod. Phys.*, 58:699, 1986.